Journal of Materials Chemistry A

ROYAL SOCIETY OF CHEMISTRY

PAPER

View Article Online
View Journal | View Issue

Cite this: *J. Mater. Chem. A*, 2020, **8**, 17670

Water assisted formation of highly oriented $CsPbI_2Br$ perovskite films with the solar cell efficiency exceeding 16%†

Ze Qing Lin, [a] Hong Wei Qiao,[a] Zi Ren Zhou,[a] Yu Hou,[a] Xiaolong Li,[b] Hua Gui Yang *[a] and Shuang Yang *[a]

Received 19th May 2020
Accepted 23rd July 2020

DOI: 10.1039/d0ta05118g

rsc.li/materials-a

Cesium lead halide perovskites are promising alternatives as light-absorbing materials for achieving perovskite solar cells with excellent thermal stability, but their inferior power conversion efficiency (PCE) and ambient instability are impeding their application. In this work, we show that liquid water can assist the formation of $CsPbI_2Br$ perovskites under the synergetic adsorption of H_2O and dimethylsulfoxide (DMSO), which enabled uniform, [100] oriented $CsPbI_2Br$ films with a grain size up to 4.4 μm. It was found that a suitable amount of H_2O helps desorb the DMSO molecules, and thus favours the formation of a cubic perovskite phase from DMSO complexed intermediates. Perovskite solar cells based on our strategy delivered an optimized PCE of 16.47% with a high open-voltage of 1.33 V, as well as good device stability against humidity, light and heat.

Introduction

Organic–inorganic hybrid halide perovskite solar cells have attracted a lot of research attention owing to their excellent photovoltaic performance and easy fabrication.[1–5] The certified power conversion efficiency (PCE) of perovskite solar cells (PSCs) has been dramatically increased from 3.8% to 25.2% in the past few years.[6–8] Despite their high efficiency, commonly studied hybrid perovskite materials are composed of volatile organic cations (*e.g.*, MA^+), leading to poor thermal and light stability.[9,10] Cesium lead halide perovskites ($CsPbX_3$, X = I, Br, Cl) are promising alternatives as light-absorbing materials for solar cell devices due to their thermal tolerance and competitive PCEs of 19.03% and 16.58% for $CsPbI_3$ and $CsPbI_2Br$ solar cells, respectively.[11–16] The growth of the PCE of $CsPbX_3$ solar cells largely depends on advancing the quality of perovskite films, which inspired the development of deposition techniques of all-inorganic perovskite thin films. So far, many fabrication methods have been developed for inorganic perovskite films, such as vacuum evaporation, multi-step deposition, spray-coating deposition, and two-step annealing fabrication.[17–20] Among these techniques, one-step solution deposition is low-cost and compatible with mass production. Unfortunately, it typically needs complicated annealing procedures because of the uncontrollable crystallization of the intermediate precursor phase.[21–23] Another critical issue is that the state-of-the-art $CsPbX_3$ cells generally adopted polycrystalline perovskite films with relatively small grains of 100–700 nm, in which the grain boundaries may hamper the device performance by causing charge recombination.[15,19,20] Previous studies on optimizing the one-step strategy mainly focused on controlling the interactions between polar solvents and non-polar anti-solvents, such as DMSO and toluene,[24] while the effects between strong liquid polar solvents have been rarely studied.

Here, we demonstrate that a small amount of liquid H_2O could trigger a synergetic crystallization process of $CsPbI_2Br$ perovskites, during which DMSO molecules are desorbed and extracted with H_2O/IPA solution from the intermediate phase, leading to pinhole-free perovskite films with a grain size up to 4.4 μm. Such a strategy realized $CsPbI_2Br$ solar cells with a high PCE of 16.47% as well as good stability under ambient, light and thermal conditions.

Results and discussion

$CsPbI_2Br$ perovskite films were deposited by a H_2O-rich solvent washing (HSW) strategy as sketched in Fig. 1a. $CsPbI_2Br$ precursor solution, dissolved in dimethyl sulfoxide (DMSO), was firstly dropped onto a compact-TiO_2/FTO substrate by spin coating. At ~55 s during spinning, the precursor film was washed with 50 μL of H_2O and isopropanol (IPA) mixed solution. A colorless intermediate phase film was immediately formed after washing with pure IPA solution, whose color did not change for over 15 min due to the strong coordination of

[a]*Key Laboratory for Ultrafine Materials of Ministry of Education, School of Materials Science and Engineering, East China University of Science and Technology, Shanghai 200237, China. E-mail: syang@sdu.edu.cn; hgyang@ecust.edu.cn*

[b]*Shanghai Synchrotron Radiation Facility, Shanghai Institute of Applied Physics, Chinese Academy of Sciences, Shanghai 201204, China*

† Electronic supplementary information (ESI) available: Experimental details, supplementary figures and tables. See DOI: 10.1039/d0ta05118g

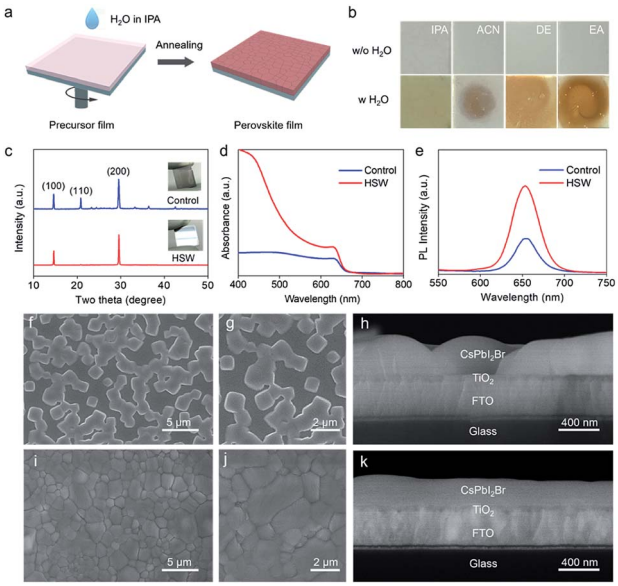

Fig. 1 (a) Schematic illustration of the HSW method. (b) Optical images of intermediate phase films treated with different solvents without (top pictures) or with (bottom ones) 1.5 vol% of H_2O. IPA, ACN, DE and EA were abbreviations of isopropanol, acetonitrile, diethyl ether and ethyl acetate, respectively. (c) XRD patterns, (d) UV-vis absorption spectra and (e) steady-state PL spectra of the as-prepared $CsPbI_2Br$ perovskite films. Insets in (c) show the photographs of the corresponding perovskite films. Perovskite layers were deposited on glass substrates for PL measurements. Top-view SEM images of the (f and g) control and (i and j) HSW $CsPbI_2Br$ perovskite films. Cross-sectional SEM images of the (h) control and (k) HSW $CsPbI_2Br$ films.

DMSO to lead ions. In contrast, a dark brown intermediate film was obtained by employing H_2O/IPA solution. To further exclude the effect of IPA on the crystallization of perovskites, we also tested another 3 solvents, including acetonitrile (ACN), ethyl acetate (EA) and diethyl ether (DE), all of which yielded colorless films without H_2O. In comparison, films washed with 1.5 vol% of H_2O became dark brown immediately, though some of them were not as uniform as the ones treated with IPA (Fig. 1b). Therefore, we conclude that H_2O is essential for promoting the formation of the perovskite phase from the DMSO complexed precursors, compared to IPA or other weak polar solvents. The intermediate films were finally annealed at 300 °C for 10 min to form $CsPbI_2Br$ perovskite films. We hereafter refer to the perovskite films prepared by IPA washing without or with 1.5 vol% H_2O as the control or HSW samples, respectively, if not specified.

X-ray diffraction (XRD) patterns in Fig. 1c showed that both control and HSW films had cubic $CsPbI_2Br$ perovskite structures with strong (100) and (200) diffraction peaks. The absence of the (110) peak of the HSW film suggested its preferred uniaxial [100] orientation. The as-deposited HSW films featured a mirror-like surface, whereas the control film was semi-transparent with weaker light absorbance (inset in Fig. 1c and d). Steady-state photoluminescence (PL) in Fig. 1e revealed about ~2.4 times PL intensity of the HSW film compared with the control one on glass substrates, which could be ascribed to the reduced charge recombination of the HSW films. Time-resolved photoluminescence (TRPL) spectra of the $CsPbI_2Br$ films in Fig. S1† exhibited biexponential decays with a fast and a slow component for both samples. The short lifetime τ_1 is normally attributed to the charge trapping procedure and the long lifetime τ_2 is related to the carrier recombination process or detrapping process.[25] The lifetime τ_1 and τ_2 were prolonged from 0.86 and 3.74 ns for the control film to 6.73 and 30.05 ns for the HSW film, confirming the considerably reduced charge recombination of the HSW film (Table S1†).

Scanning electron microscopy (SEM) was performed to investigate the surface microscopic morphologies of the $CsPbI_2Br$ films. The control film exhibited a rough surface and micron-sized crystals with low coverage of the TiO_2/FTO substrates (Fig. 1f–h and S2a†). In striking contrast, the HSW film presented a compact and uniform pinhole-free morphology with negligible reduction in the grain size (Fig. 1i–k). A mean grain size of 1.7 μm was obtained for the HSW film, with the largest size of 4.4 μm, as also manifested by the atomic force microscopy (AFM) characterization (Fig. S2b and S3†). Since IPA may weakly coordinate with the $CsPbI_2Br$ precursor and affect the crystallization process, we also fabricated a $CsPbI_2Br$ film without IPA washing (Fig. S4†).[26] The annealed film exhibited a similar surface morphology to the control film, again validating the important role of H_2O for the formation of high-quality $CsPbI_2Br$ films.

The aforementioned results have confirmed the water effect on perovskite crystallization; we then explored the influence of the H_2O concentration on the resultant $CsPbI_2Br$ perovskite films. The most notable phenomenon by using different H_2O concentrations was the color change of the intermediate products; the color of films clearly changed from colorless to dark brown and then faded to pale yellow with the H_2O volume ratio from 0% to 40% (Fig. 2a). It is apparent that there is a large window for the H_2O volume from 0.5% to 30% to promote the formation of perovskite crystals, though excess H_2O can dissolve CsI with less soluble PbI_2 or hydrates.[27] For the films formed without H_2O, the intermediate films would course into dynamically favored island shaped films (Fig. S4†). Increasing the H_2O concentration to 1.5 vol% would facilitate the individual particles to join together for forming pinhole-free films (Fig. 2b and c). At 3 vol% of H_2O, the surface of perovskite films became rough with convex shaped grains (Fig. 2d). When 5 vol% of H_2O was used, linearly shaped grains appeared and stacked on the film (Fig. 2e). The coverage of these perovskite films was also reflected by UV-vis spectra in Fig. S5.† Since the rough surface is not suitable for device applications, the H_2O volume ratio used in this study is controlled below 5%. It was noteable that there was a slight decrease in average grain sizes from 2.2 to 1.1 μm by increasing the H_2O concentration from 0% to 5% (Fig. 2f). The aspect ratio of the grains in the as-prepared films was further analyzed, which initially increased, and then reduced with a maximum value of 5.67 at a H_2O concentration of 1.5 vol% (Fig. 2g and S6†). The XRD patterns in Fig. 2h ascertained the pure cubic perovskite phase of all samples. It can be found that the (110) peak intensity of all samples decreased with the use of H_2O solution and the (110) peak is almost negligible in the film at a H_2O concentration of 1.5 vol%,

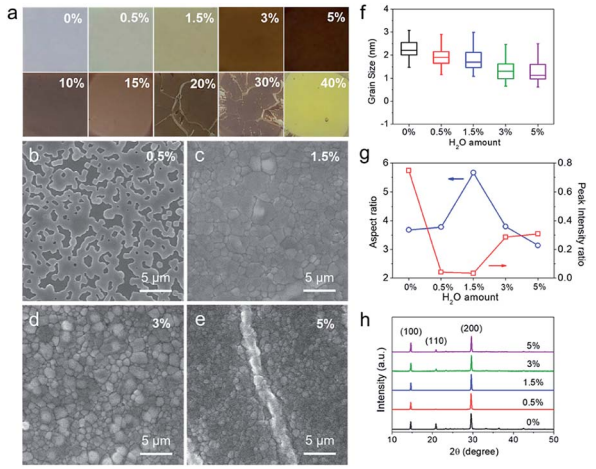

Fig. 2 (a) Optical images of the intermediate phase films obtained from isopropanol solution washing with different volume ratios of H_2O. The darkening of the films implied the formation of a black perovskite phase. (b–e) Top-view SEM images and (f) grain size distribution of $CsPbI_2Br$ films obtained from the HSW route with different concentrations of H_2O. (g) Dependence of the (110)/(100) peak intensity ratio and average aspect ratio of $CsPbI_2Br$ films on the H_2O concentration of the HSW methods. The aspect ratio is defined by the ratio between the grain size and the thickness of the as-prepared films. (h) XRD patterns of $CsPbI_2Br$ films obtained from the HSW route with different concentrations of H_2O.

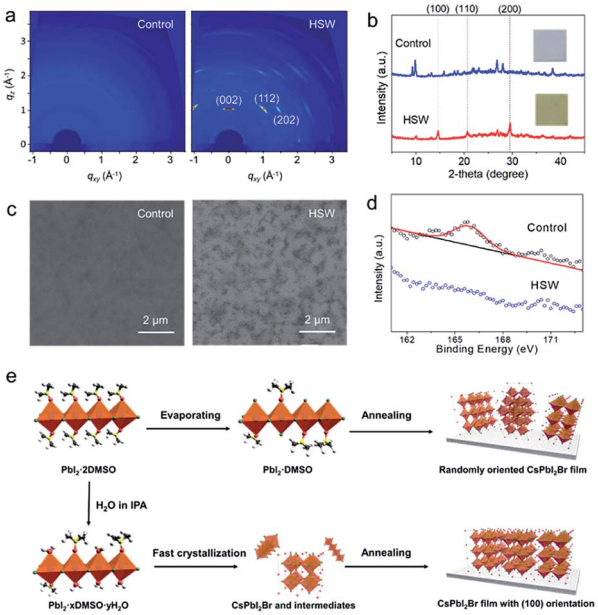

Fig. 3 (a) GIWAXS, (b) XRD patterns, (c) SEM images and (d) XPS S 2p spectra of $CsPbI_2Br$ intermediate phase films with and without H2O washing. (e) Plausible formation mechanisms of $CsPbI_2Br$ perovskite films.

indicating that suitable amounts of H_2O would favor the oriented growth of $CsPbI_2Br$ films along the [100] crystallographic axis.

To further examine the role of H_2O during the HSW process, we scrutinized the intermediate phase film by grazing-incidence wide-angle X-ray scattering (GIWAXS), XRD, XPS and SEM measurements. The GIWAXS was measured in a N_2 filled chamber and tested right after spin coating (Fig. S7†). As described in Fig. 3a, the control intermediate film presented very weak diffraction rings without any spots, which should be dominated by the amorphous phase. As a comparison, the HSW sample shows the (002), (112) and (202) scattering spots of cubic $CsPbI_2Br$ perovskite, in good agreement with the XRD patterns (Fig. 3b). Additionally, the intermediate phase of the control film was indexed as $PbI_2 \cdot DMSO$.[28] It should be pointed out that the XRD tests were carried out after the film deposition for about 10 min with an aging process, which led to the difference between GIWAXS results. According to the above results, we can reasonably conclude that a strong coordination effect of DMSO retards the formation of the perovskite phase; the colloidal intermediate phase is strongly adsorbed by DMSO molecules, and slowly reconstructed to a thermodynamically favored perovskite crystals with a cubic morphology during the drying and annealing process. However, liquid H_2O could extract and partially substitute the adsorbed DMSO molecules from the $PbI_2 \cdot DMSO$ complex by breaking the O–Pb bond, upon which the oligomers readily aggregated into bulk perovskites (Fig. 3e).[29] The removal of DMSO by H_2O was further corroborated by XPS S 2p spectra in Fig. 3d which shows that the HSW films present negligible sulfur signals compared to the control one. Therefore, the soft intermediate phase was rapidly solidified into compact perovskite films with only few intermediate products under the synergetic effect of DMSO and H_2O. This was also evidenced by the SEM images of intermediate films before annealing (Fig. 3c), in which the dark and bright regions of HSW films should be the perovskite and intermediate phases, respectively.

Solar cells structured as FTO/c-TiO_2/perovskite/P3HT/Au were fabricated based on the HSW $CsPbI_2Br$ film. The cross-sectional SEM image of a typical device with the HSW

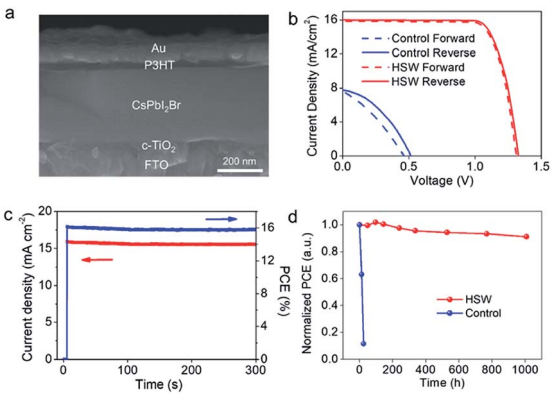

Fig. 4 (a) Cross-sectional SEM image of a typical solar cell device. The perovskite layer was deposited by the HSW method. (b) *J–V* curves of perovskite devices measured under simulated AM 1.5G irradiation under different scan directions. (c) Steady-state measurements of the photocurrent density and PCE of the champion device with the HSW perovskite layer held at a MPP voltage of 1.04 V. (d) Long-term stability measurements of unencapsulated PSCs. The device was stored in ambient air with a relative humidity of 15 ± 3%.

perovskite layer is shown in Fig. 4a. The thickness of the $CsPbI_2Br$ layer is estimated to be ~300 nm. Importantly, no grain boundaries could be observed throughout the whole perovskite layer, suggestive of large single crystalline domains. The energy levels of $CsPbI_2Br$ were determined from the UPS spectra and Tauc plots of UV-vis spectra (Fig. S8 and S9†), and the schematic energy level alignment of the device is depicted in Fig. S10.† The optimal H_2O concentration was confirmed to be 1.5 vol% according to the photovoltaic performance (Fig. S11 and Table S2†). The control devices exhibited a short-current density (J_{SC}) of 7.77 mA cm^{-2}, an open-circuit voltage (V_{OC}) of 0.515 V, and a fill factor (FF) of 0.38, leading to a PCE of 1.52%. The performance improved significantly by using the HSW strategy; a highest efficiency of 16.47% was reached for the $CsPbI_2Br$ film with the optimized H_2O volume ratio of 1.5%, with a J_{SC} of 15.98 mA cm^{-2}, a V_{OC} of 1.33 V, and a FF of 0.78 (Fig. 4b). Almost no photocurrent hysteresis was found between the forward and reverse scans (Table S3†). Noteworthily, our device efficiency is competitive among the highest PCEs of the reported $CsPbI_2Br$ solar cells (Table S4†). The external quantum efficiency (EQE) spectra of the control and HSW cells in Fig. S12† delivered an integrated J_{SC} of 7.33 mA cm^{-2} and 15.67 mA cm^{-2} respectively, in good agreement with the *J–V* results. Furthermore, a stabilized efficiency of 15.76% was achieved with a stabilized photocurrent of 15.53 mA cm^{-2} under the maximum power output voltage of 1.04 V, confirming the reliability of *J–V* measurements (Fig. 4c). The good reproducibility of the HSW method was illustrated by measuring over 20 individual devices whose average V_{OC} and PCE were found to be 1.31 $\pm$ 0.01 V and 15.91 $\pm$ 0.36%, respectively (Fig. S13†). In contrast, the control cells only gave an average V_{OC} and PCE of 0.46 $\pm$ 0.07 V and 0.94 $\pm$ 0.38%, respectively.

To quantitatively assess the defect density and mobility of $CsPbI_2Br$ films, we performed space-charge limited current (SCLC) measurements (Fig. S14†).[30,31] The electron-only device structure is FTO/TiO_2/$CsPbI_2Br$/PCBM/Ag. Trap densities ($N_{defects}$) could be calculated according to the following equation $N_{defects} = 2\varepsilon\varepsilon_0 V_{TFL}/eL^2$, where V_{TFL} is the trap-fill limit voltage, ε and ε_0 are the dielectric constant of $CsPbI_2Br$ and the vacuum permittivity, respectively, L is the thickness of the $CsPbI_2Br$ film, and e is the electron charge. The value of V_{TFL} for the HSW $CsPbI_2Br$ films was 1.24 V, which corresponded to the electron trap density of 6.2 $\times$ 10^{16} cm^{-3}. The electron mobility was calculated according to Mott–Gurney's equation $\mu = (8JL^3)/(9\varepsilon\varepsilon_0 V^2)$. The electron mobility was estimated to be 1.03 cm^2 V^{-1} s^{-1}, which is among the best of this type of perovskite.[32,33] In contrast, the control $CsPbI_2Br$ device delivered a larger trap density of 9.7 $\times$ 10^{16} cm^{-3} and a lower electron mobility of 0.34 cm^2 V^{-1} s^{-1}.

Cesium lead halide perovskites have been reported to be particularly unstable under moisture conditions, compared with their organic–inorganic counterparts.[34] We stored the perovskite films in ambient air with a relative humidity of 15 $\pm$ 3% at room temperature. We found that the HSW film was stable over 7 days, while the control one almost fully degraded within 1 day (Fig. S15†). The enhanced ambient stability may be derived from the better crystallinity as showed in previous reports.[35] A solar cell device based on the HSW perovskite layer was also subjected to ambient conditions for over 1000 h and the PCE of our device maintained over 90% of its original value (Fig. 4d). In contrast, the control $CsPbI_2Br$ device exhibited a much faster degradation rate, delivering almost no photovoltaic performance after 24 hours. The operational stability and thermal stability of the control and HSW $CsPbI_2Br$ devices were also measured, as shown in Fig. S16.† Without encapsulation, the HSW device maintained 94% of its initial efficiency after 400 h under continuous AM 1.5G light soaking while the PCE of the control device almost lost 28% of the initial efficiency. Moreover, the HSW solar cell lost <8% of its initial PCE over within 200 h at 85 °C under nitrogen. The control device only maintained 71% of its initial efficiency under the same conditions. The good long-term device stability again highlights the merits of high-quality $CsPbI_2Br$ perovskite layers processed by the HSW method.

Conclusions

In summary, we developed a new approach to fabricate large grain-sized $CsPbI_2Br$ films with a preferred [100] orientation. It was found that a certain amount of H_2O can initiate a synergetic process to mediate the coordination chemistry and solidify the intermediate film into fully covered perovskite films. A solar cell device based on this strategy achieved a high PCE of 16.47% *via* the HSW strategy, which is competitive among the pervious reported high-efficiency $CsPbI_2Br$ devices. Importantly, the device can maintain over 90% of its initial efficiency for 1000 h of storage under ambient conditions with a humidity of 15 $\pm$ 3%, and maintained ~93% of its initial efficiency after 500 h under continuous AM 1.5G light soaking. The incorporated H_2O in the HSW process is expected to screen the effect of moisture form air, as the employed H_2O concentration is much higher. Our preliminary results have also shown the feasibility of fabricating cells by the HSW strategy under ambient conditions. This work offers a new pathway for tuning the crystallization kinetics of all-inorganic perovskites and may serve a wide range of halide perovskite devices.

Conflicts of interest

There are no conflicts to declare.

Acknowledgements

This work was financially supported by the National Natural Science Funds for Distinguished Young Scholar (51725201), National Natural Science Foundation of China (51972111, 51902185, and 51602103), Young Elite Scientists Sponsorship Program by CAST (2017QNRC001), International (Regional) Cooperation and Exchange Projects of the National Natural Science Foundation of China (51920105003), Innovation Program of Shanghai Municipal Education Commission (E00014), Fundamental Research Funds for the Central Universities (JKD012016025, and JKD012016022) and Shanghai Engineering Research Center of Hierarchical Nanomaterials (18DZ2252400).

The authors thank beamline BL14B1 at the Shanghai Synchrotron Radiation Facility (SSRF) for providing the beam time.

Notes and references

1 H.-S. Kim, C.-R. Lee, J.-H. Im, K.-B. Lee, T. Moehl, A. Marchioro, S.-J. Moon, R. Humphry-Baker, J.-H. Yum, J. E. Moser, M. Grätzel and N.-G. Park, *Sci. Rep.*, 2012, **2**, 591.
2 M. M. Lee, J. Teuscher, T. Miyasaka, T. N. Murakami and H. J. Snaith, *Science*, 2012, **338**, 643–646.
3 S. Yang, S. Chen, E. Mosconi, Y. Fang, X. Xiao, C. Wang, Y. Zhou, Z. Yu, J. Zhao, Y. Gao, F. D. Angelis and J. Huang, *Science*, 2019, **365**, 473–478.
4 W. S. Yang, J. H. Noh, N. J. Jeon, Y. C. Kim, S. Ryu, J. Seo and S. I. Seok, *Science*, 2015, **348**, 1234–1237.
5 S. Yang, J. Dai, Z. Yu, Y. Shao, Y. Zhou, X. Xiao, X. C. Zeng and J. Huang, *J. Am. Chem. Soc.*, 2019, **141**, 5781–5787.
6 A. Kojima, K. Teshima, Y. Shirai and T. Miyasaka, *J. Am. Chem. Soc.*, 2009, 6050–6051.
7 H. W. Qiao, S. Yang, Y. Wang, X. Chen, T. Y. Wen, L. J. Tang, Q. Cheng, Y. Hou, H. Zhao and H. G. Yang, *Adv. Mater.*, 2019, **31**, e1804217.
8 National Renewable Energy Laboratory, *Best Research-Cell Efficiency Chart*, https://www.nrel.gov/pv/assets/pdfs/best-research-cell-efficiencies.20200406.pdf.
9 G. E. Eperon, S. D. Stranks, C. Menelaou, M. B. Johnston, L. M. Herz and H. J. Snaith, *Energy Environ. Sci.*, 2014, **7**, 982–988.
10 T. Leijtens, G. E. Eperon, N. K. Noel, S. N. Habisreutinger, A. Petrozza and H. J. Snaith, *Adv. Energy Mater.*, 2015, **5**, 1500963.
11 J. Song, J. Li, X. Li, L. Xu, Y. Dong and H. Zeng, *Adv. Mater.*, 2015, **27**, 7162–7167.
12 W. Chen, J. Zhang, G. Xu, R. Xue, Y. Li, Y. Zhou, J. Hou and Y. Li, *Adv. Mater.*, 2018, **30**, 1800855.
13 J. Lin, M. Lai, L. Dou, C. S. Kley, H. Chen, F. Peng, J. Sun, D. Lu, S. A. Hawks, C. Xie, F. Cui, A. P. Alivisatos, D. T. Limmer and P. Yang, *Nat. Mater.*, 2018, **17**, 261–267.
14 Z. Wei and J. Xing, *J. Phys. Chem. Lett.*, 2019, **10**, 3035–3042.
15 Y. Wang, X. Liu, T. Zhang, X. Wang, M. Kan, J. Shi and Y. Zhao, *Angew. Chem., Int. Ed.*, 2019, **58**, 16691–16696.
16 J. Xue, R. Wang, K. L. Wang, Z. K. Wang, I. Yavuz, Y. Wang, Y. Yang, X. Gao, T. Huang, S. Nuryyeva, J. W. Lee, Y. Duan, L. S. Liao, R. Kaner and Y. Yang, *J. Am. Chem. Soc.*, 2019, **141**, 13948–13953.
17 P. Becker, J. A. Márquez, J. Just, A. Al-Ashouri, C. Hages, H. Hempel, M. Jošt, S. Albrecht, R. Frahm and T. Unold, *Adv. Energy Mater.*, 2019, **9**, 1900555.
18 J. Duan, Y. Zhao, B. He and Q. Tang, *Angew. Chem., Int. Ed.*, 2018, **57**, 3787–3791.
19 C.-F. J. Lau, X. Deng, Q. Ma, J. Zheng, J. S. Yun, M. A. Green, S. Huang and A. W. Y. Ho-Baillie, *ACS Energy Lett.*, 2016, **1**, 573–577.
20 C. Liu, W. Li, C. Zhang, Y. Ma, J. Fan and Y. Mai, *J. Am. Chem. Soc.*, 2018, **140**, 3825–3828.
21 B. Li, M. Li, C. Fei, G. Cao and J. Tian, *J. Mater. Chem. A*, 2017, **5**, 24168–24177.
22 M. Xiao, F. Huang, W. Huang, Y. Dkhissi, Y. Zhu, J. Etheridge, A. Gray-Weale, U. Bach, Y.-B. Cheng and L. Spiccia, *Angew. Chem., Int. Ed.*, 2014, **53**, 9898–9903.
23 H. Choi, K. Choi, Y. Choi, T. Kim, S. Lim and T. Park, *Small Methods*, 2019, 1900569, DOI: 10.1002/smtd.201900569.
24 N. J. Jeon, J. H. Noh, Y. C. Kim, W. S. Yang, S. Ryu and S. I. Seok, *Nat. Mater.*, 2014, **13**, 897–903.
25 M. Maiberg, T. Hölscher, S. Zahedi-Azad and R. Scheer, *J. Appl. Phys.*, 2015, **118**, 105701.
26 W. Chen, H. Chen, G. Xu, R. Xue, S. Wang, Y. Li and Y. Li, *Joule*, 2019, **3**, 191–204.
27 Y.-H. Kye, C.-J. Yu, U.-G. Jong, Y. Chen and A. Walsh, *J. Phys. Chem. Lett.*, 2018, **9**, 2196–2201.
28 G. Yin, H. Zhao, H. Jiang, S. Yuan, T. Niu, K. Zhao, Z. Liu and S. F. Liu, *Adv. Funct. Mater.*, 2018, **28**, 1803269.
29 K. Zhang, Z. Wang, G. Wang, J. Wang, Y. Li, W. Qian, S. Zheng, S. Xiao and S. Yang, *Nat. Commun.*, 2020, **11**, 1006.
30 Z. Liu, J. Hu, H. Jiao, L. Li, G. Zheng, Y. Chen, Y. Huang, Q. Zhang, C. Shen, Q. Chen and H. Zhou, *Adv. Mater.*, 2017, **29**, 1606774.
31 Q. Dong, Y. Fang, Y. Shao, P. Mulligan, J. Qiu, L. Cao and J. Huang, *Science*, 2015, **347**, 967–970.
32 J. Lu, S.-C. Chen and Q. Zheng, *Sci. China: Chem.*, 2019, **62**, 1044–1050.
33 Z. Ye, J. Zhou, J. Hou, F. Deng, Y.-Z. Zheng and X. Tao, *Sol. RRL*, 2019, **3**, 1900109.
34 M. B. Faheem, B. Khan, C. Feng, M. U. Farooq, F. Raziq, Y. Xiao and Y. Li, *ACS Energy Lett.*, 2020, **5**, 290–320.
35 Q. Wang, B. Chen, Y. Liu, Y. Deng, Y. Bai, Q. Dong and J. Huang, *Energy Environ. Sci.*, 2017, **10**, 516–522.

